JOURNAL OF GEOPHYSICAL RESEARCH, VOL. 113, D18202, doi:10.1029/2008JD010246, 2008

Remote sensing of mineral dust aerosol using AERI during the UAE^2: A modeling and sensitivity study

R. A. Hansell,[1,2] K. N. Liou,[1] S. C. Ou,[1] S. C. Tsay,[3] Q. Ji,[4] and J. S. Reid[5]

Received 9 April 2008; revised 9 June 2008; accepted 24 June 2008; published 17 September 2008.

[1] Numerical simulations and sensitivity studies have been performed to assess the potential for using brightness temperature spectra from a ground-based Atmospheric Emitted Radiance Interferometer (AERI) during the United Arab Emirates Unified Aerosol Experiment (UAE^2) for detecting/retrieving mineral dust aerosol. A methodology for separating dust from clouds and retrieving the dust IR optical depths was developed by exploiting differences between their spectral absorptive powers in prescribed thermal IR window subbands. Dust microphysical models were constructed using in situ data from the UAE^2 and prior field studies while composition was modeled using refractive index data sets for minerals commonly observed around the UAE region including quartz, kaolinite, and calcium carbonate. The T-matrix, finite difference time domain (FDTD), and Lorenz-Mie light scattering programs were employed to calculate the single scattering properties for three dust shapes: oblate spheroids, hexagonal plates, and spheres. We used the Code for High-resolution Accelerated Radiative Transfer with Scattering (CHARTS) radiative transfer program to investigate sensitivity of the modeled AERI spectra to key dust and atmospheric parameters. Sensitivity studies show that characterization of the thermodynamic boundary layer is crucial for accurate AERI dust detection/retrieval. Furthermore, AERI sensitivity to dust optical depth is manifested in the strong subband slope dependence of the window region. Two daytime UAE^2 cases were examined to demonstrate the present detection/retrieval technique, and we show that the results compare reasonably well to collocated AERONET Sun photometer/MPLNET micropulse lidar measurements. Finally, sensitivity of the developed methodology to the AERI's estimated MgCdTe detector nonlinearity was evaluated.

Citation: Hansell, R. A., K. N. Liou, S. C. Ou, S. C. Tsay, Q. Ji, and J. S. Reid (2008), Remote sensing of mineral dust aerosol using AERI during the UAE^2: A modeling and sensitivity study, *J. Geophys. Res.*, *113*, D18202, doi:10.1029/2008JD010246.

1. Introduction

[2] The effect of mineral dust on the Earth's climate system remains highly uncertain [*Intergovernmental Panel on Climate Change*, 2007] due in part to a lack of reliable data and a comprehensive understanding of its complex radiative properties, particularly in the thermal IR where common dust minerals exhibit a wide range of spectral features [*Sokolik and Toon*, 1999]. Exploiting the longwave properties of dust for the purpose of measuring and modeling high-resolution dust spectra has been the focus of recent research efforts [*DeSouza-Machado et al.*, 2006; *Hong et al.*, 2006; *Pierangelo et al.*, 2004, 2005]. Although significant progress has been made, accurate dust parameterizations for remote sensing and climate applications will strongly depend on the availability of quality global dust data (e.g., size and shape parameters, mineral composition, spectral refractive indices, etc) from major source regions around the world.

[3] In response to the need for dust data, there has been a large increase in field studies designed to measure key dust properties in areas affected by dust aerosol. One such study, the United Arab Emirates Unified Aerosol Experiment (UAE^2), was conducted from August to September 2004. During the UAE^2, over two dozen research organizations convened in the United Arab Emirates (UAE) to participate in field experiments designed to include the following objectives: (1) to provide ground truth for satellite and model products in the region's highly heterogeneous environment, (2) to evaluate the properties of dust particles from the numerous sources that converge in the UAE region, (3) to determine the impact of aerosol particles on the local radiation budget, and (4) to determine the effect of the radiative perturbations on regional mesoscale flow patterns.

[4] The primary ground sites deployed during the UAE^2 were: the Naval Research Laboratory's Mobile Atmospheric

[1]Department of Atmospheric and Oceanic Sciences, University of California, Los Angeles, California, USA.
[2]Now at Earth System Science Interdisciplinary Center, University of Maryland, College Park, Maryland, USA.
[3]NASA Goddard Space Flight Center, Greenbelt, Maryland, USA.
[4]Earth System Science Interdisciplinary Center, University of Maryland, College Park, Maryland, USA.
[5]Naval Research Laboratory, Monterey, California, USA.

0148-0227/08/2008JD010246$09.00

Aerosol and Radiation Characterization Observatory (MAARCO) located along the coast approximately 60 km northeast of Abu Dhabi at (24°N; 54°E) and the NASA Goddard Space Flight Center's Surface-sensing Measurements for Atmospheric Radiative Transfer (SMART) located in the interior desert at Al-Ain airport near (24°N; 55°E) just west of Oman. Both sites were strategically located to include the UAE coastal and desert regions to provide comprehensive instrumental coverage for measuring both aerosol properties and surface radiation. The UAE^2 hosted a diverse array of instrumentation both at the surface and onboard aircraft and satellite platforms. Among the ground-based instruments deployed was the SMART Atmospheric Emitted Radiance Interferometer (AERI) which has much potential for dust remote sensing applications. The AERI's high spectral resolution allows us to exploit the absorptive differences of dust minerals across prescribed thermal IR "clean" window subbands enabling the differentiation of dust from cirrus and liquid water clouds and the retrieval of dust IR optical depths. AERI has been used by previous investigators for providing near-continuous profiling of temperature, moisture and atmospheric stability [*Feltz et al.*, 2003], cloud phase determination and retrieval of cloud properties [*Turner et al.*, 2003], measuring cirrus cloud visible-to-infrared spectral optical depth ratios [*Deslover et al.*, 1999], evaluating surface aerosol IR forcing [*Vogelmann et al.*, 2003], and measuring IR emissions from the Saharan Air Layer (SAL [*Nalli et al.*, 2006]) using the M-AERI system, an IR spectroradiometer designed for shipboard applications.

[5] This paper investigates the potential for detecting and retrieving airborne mineral dust properties using AERI brightness temperature (BT) spectra with applications to the UAE^2 field experiment. To this end, detailed sensitivity studies of the modeled spectra to key dust and atmospheric parameters are examined which include dust particle size and shape, dust optical depth, dust layer thickness and altitude, and the vertical distributions of water vapor and temperature. A methodology has been developed for detecting/separating dust from cloud and retrieving the dust IR optical depths. The physical basis for the approach relies on the complex spectral variability of the IR optical properties for common mineral dust components. Dust detection follows the physical principles of dust and cloud particle absorption across the thermal IR window, while the retrieval scheme employs a χ^2 statistical optimization approach in the AERI "clean" subbands for determining the dust IR optical depths. The dynamical state of the column atmosphere is accounted for by combining the AERI retrieved temperature and moisture profiles from the University of Wisconsin, Space Science and Engineering Center's (UW-SSEC) AERIPLUS physical retrieval algorithm [*Feltz et al.*, 2003] with regional sounding data using the MAARCO radiosondes. To illustrate the detection and retrieval methodology, AERI data from two daytime UAE^2 cases were evaluated. Case 1 demonstrates the method's ability to successfully separate dust from cirrus clouds under mostly cloudy skies, while case 2 illustrates the retrieval of dust optical depths during typical dust conditions. The preliminary results are then compared to the collocated Micropulse Lidar Network (MPLNET) micropulse lidar and Aerosol Robotic Network (AERONET) Sun photometer measurements. Detection and retrieval errors due to the estimated AERI mercury-cadmium-telluride (MgCdTe) detector nonlinearity are also evaluated. Application of the current methodology using the UAE^2 AERI data set corrected for the detector nonlinearity will be discussed in a following paper with implications for computing the dust longwave surface radiative forcing. Although the UAE^2 AERI measurements are daytime only, the technique can also be applied to nighttime measurements. Potential research areas that may benefit include daytime and nighttime dust hazard mitigation, assessment of the diurnal effects of regional dust surface radiative forcing, and validating satellite-based dust aerosol remote sensing products.

[6] This paper is organized as follows. Section 2 discusses dust microphysics and single-scattering properties in the thermal IR window, and the structure of the radiative transfer model. Section 3 details the sensitivity studies to key dust and atmospheric parameters, the estimated MgCdTe detector nonlinearity error, and the model atmosphere and clear-sky spectra. The AERI detection and retrieval methodology along with two UAE^2 case studies with and without estimated nonlinearity error corrections applied are examined in section 4 and lastly, a summary is given in section 5.

2. Dust Microphysics and Single-Scattering Properties in the Thermal IR Window

[7] Conventional approaches for calculating dust's single-scattering properties in the thermal IR window depend on a priori knowledge and/or assumptions about dust composition, shape and size distributions. The following describes the modeling of each key dust parameter, and its implementation in the current study along with the theoretical basis and rationale.

2.1. Dust Composition

[8] Individual dust particles are usually mixtures of different types of minerals. These include silicates, such as quartz and clays (e.g., kaolinite, montmorillinite and illite), and nonsilicates, which include carbonates (e.g., calcite and dolomite), iron oxides (e.g., hematite and magnetite) and sulfates (e.g., gypsum). Significant work in modeling dust composition has been performed by *Sokolik and Toon* [1999] and *Kalashnikova and Sokolik* [2004].

[9] To model dust composition for application to AERI dust detection/retrieval during the UAE^2, we employed the refractive indices of typical minerals observed around the UAE region, consisting of pure silicates (mainly quartz) and clays (kaolinite and illite). We selected quartz and kaolinite to be the major components of dust, since quartz is often found to be dominant in terms of mass [*Sokolik and Toon*, 1999] and the mineralogical composition of clay-size mode particles collected from Saudi Arabia, which is just south of UAE, were found to contain kaolinite at approximately 55% by weight [*Sokolik and Toon*, 1999]. Studies of airborne dust properties in other nearby regions [*Singer et al.*, 2004] also show quartz and kaolinite to be dominate mineral species in collected dust samples. Illite is also evaluated on the basis of work performed by *Aba-Husayn and Sayegh* [1977]. Last, to consider particles with a heterogeneous composition, we investigated dust mixtures consisting of hematite (10%) and calcium carbonate (50%) internally

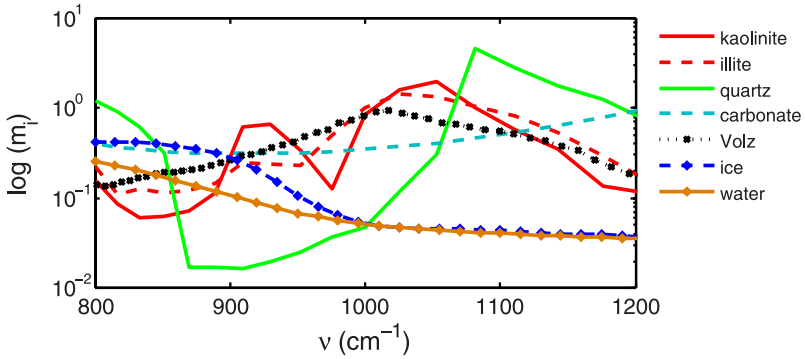

Figure 1. Log plot of the imaginary components (m_i) of the complex refractive index for common dust minerals versus liquid water and ice in the thermal IR window. Calcium carbonate is scaled 100 times for comparison.

mixed with kaolinite and quartz. The calcium carbonate was used to account for the large distributions of distinct limestone sources found throughout the UAE region [*Reid et al.*, 2008] and hematite for the possibility of traces of iron oxide in the soil. The Bruggemann effective medium approximation was used to calculate the refractive indices of internally mixed dust minerals [*Sokolik and Toon*, 1999]. Back trajectories from a kinetic trajectory code, provided by NASA-GSFC and made available by the AERONET program [*Holben et al.*, 1998], show evidence for Saharan dust in the UAE region. For this reason, the *Volz* [1973] refractive indices were employed to represent transported Saharan desert dust.

[10] Figure 1 is a log plot of the imaginary components of the complex refractive index for common dust minerals in the thermal IR window (800–1200 cm^{-1}). In the wavelength domain, the window region corresponds to 8–12 μm; however for the remainder of the paper, we will continue to use wave number when referring to AERI spectra. For convenience, the curves are color coded according to mineral class, i.e., red for clays, green for quartz, and light blue for carbonate. The refractive indices from the *Volz* [1973] bulk dust sample (black) are shown for comparison. Note the large spectral variability between mineral classes, whereas for the bulk dust sample, the spectrum is smoothed out because of internal mixing of the component minerals. Unlike liquid water (orange) and ice (blue), minerals have strong absorption features due to their dominant molecular vibrational motions. The differences in the refractive indices between minerals and liquid water and ice in the thermal IR widow form the basis for this paper's dust/cloud detection technique.

2.2. Dust Size and Shape Distributions

2.2.1. Particle Size

[11] Particle size is a crucial parameter over which the single-scattering properties for individual sizes and shapes are integrated to yield bulk dust optical properties. In this study, dust particle sizes were characterized by using synthesized lognormal size distributions, based on size parameters obtained from the UAE^2 MAARCO aerodynamical particle sizer (APS 3321) data set [*Reid et al.*, 2008].

[12] For unique APS size groups that were found to be characteristic of specific dust source regions, the volume median diameters (VMD) and their geometric standard deviations (σ_{gv}) were identified [*Reid et al.*, 2008]. Each of these groups was associated with a specific source location. The average VMD and σ_{gv} were 3.8 ± 0.4 μm and 2.0 ± 0.1, μm respectively. To account for the possibilities of fine and coarse mode dust at SMART, the range of VMDs were extended to include smaller (VMD = 1.5 μm) and larger (VMD = 10 μm) sized particles each with a σ_{gv} = 1.9–2.0. The effective size range employed in this study was r_{eff} = 0.75–5.0 μm. Since the AERI retrieved IR optical depths will be dominated more significantly by the presence of coarse-mode dust as compared to the fine-mode influence in the visible wavelengths, the extended range of size parameters is significant for determining, if any, the sensitivity of the AERI BT spectra to particle size. Details are given in section 3. The size distributions were constructed using the averaged integrated coarse-mode (0.8–10 μm) dust particle concentrations above 200 μm^3 cm^{-3} which corresponded to 16 dust events including one of the largest that occurred on 12 September 2004 [*Reid et al.*, 2008].

2.2.2. Particle Shape

[13] Dust particles are rarely spherical as evidenced from numerous prior works [e.g., *Okada et al.*, 1987, 2001; *Parungo et al.*, 1995; *Koren et al.*, 2001; *Reid et al.*, 2003] which show that as dust particle size increases as in the case of heavy dust outbreaks, so too does its circularity (ratio of particle's perimeter to its cross-sectional area), a dimensionless parameter for measuring the particle's deviation from a perfect sphere. This study used both spherical and nonspherical dust particles for examining the sensitivity to dust and atmospheric parameters. To investigate the effect of sharp-edged dust particles, a single randomly oriented particle geometry involving a hexagonal flat plate (i.e., compact hexagonal column) was chosen to represent clay particles with an aspect ratio L/2A of 1, where L is the axial length parameter and A is the half width. Table 1 gives the L and A values used in the calculation based on the volume-equivalent spherical radii of 0.1, 1.0 and 2.5 μm.

[14] We also assumed dust particles are randomly oriented, rotationally symmetric oblate spheroids following the work of *Reid et al.* [2003] and *Okada et al.* [2001] who found typical aspect ratios for dust particles to be in the range of 1.4–1.9, on the basis of samples collected during PRIDE and in China, respectively. Aspect ratio distributions from PRIDE [*Reid et al.*, 2003], which preliminarily seem

Table 1. FDTD Size Parameters

Volume-Equivalent Spherical Radius (μm)	L (μm)	A (μm)
0.1	0.148	0.296
1.0	1.48	2.95
2.5	3.69	7.39

to match the findings during the UAE^2 field campaign, were used in this study to account for the range of particle shapes when calculating the dust single-scattering properties. *Reid et al.* [2003] found the aspect ratios to be large and broad-based with median values averaging 1.9 ± 0.9 with the largest particles (>10 μm) representing approximately 3% of the sampled population.

2.3. Dust Single-Scattering Properties

[15] The classical approach for computing dust single-scattering properties is to assume that dust particles are spheres so that the Lorenz-Mie scattering code can be applied. The nonspherical and irregular nature of dust particles however, demands that a more detailed light-scattering code capable of resolving the nonspherical particle geometry be employed for determining the single-scattering properties. Several such codes are available. The T-matrix method [*Waterman*, 1971; *Mishchenko and Travis*, 1994], an analytical approach to light scattering, is useful for simulating spheroids, circular cylinders and Chebyshev particles. For this study, we treat dust particles as oblate spheroids in which the shape and size parameters are specified by the aspect ratio (a/b, ratio of the horizontal to vertical semiaxis) and the radius of an equal volume sphere, r_v. Dust particles with extremely large aspect ratios and imaginary refractive indices or large sizes may cause the T-matrix method to produce unrealistic results (e.g., single-scattering albedos $\varpi > 1$) or fail to converge [*Mishchenko and Travis*, 1998]. The T-matrix code's sensitivity to these extreme parameters was evaluated by iteratively calculating the single-scattering properties for a range of particle aspect ratios, compositions, and sizes over the window region. It was found that using common silicate minerals with a/b < 4.0 for the size range employed in this study yields physically realistic single-scattering properties in the thermal IR window. When particle asphericity was further increased, the T-matrix method failed to converge, most likely because of numerical instability caused by extreme values in the particle parameters [*Mishchenko and Travis*, 1998]. To ensure the physical correctness of the computed results and for consistency with observed shape parameter data, the single-scattering properties were integrated over a more moderate range of aspect ratios from 1.2 to 2.2 for particles that are nearly spherical to those that are elongated (oblate) spheroids. We also employ the finite difference time domain method (FDTD [*Yee*, 1966; *Yang and Liou*, 1995]), which is a numerical approach for simulating light scattering by particles of more complicated shapes. For this study, dust particles were represented as compact hexagonal columns (i.e., flat plate-like structures [*Reid et al.*, 2003]), similar to the common clay kaolinite [*Kalashnikova and Sokolik*, 2004].

[16] Both the T-matrix and FDTD methods were used to calculate the single-scattering properties for individual particle sizes and shapes over the thermal IR window based on observed dust parameters. The single-scattering properties include the extinction and scattering coefficients (β_e and β_s), the single-scattering albedo (ϖ), and the asymmetry parameter (g). We integrated β_e, β_s, ϖ, and g over the UAE^2-APS size distributions and the aspect ratio shape distributions from PRIDE [*Reid et al.*, 2003] across the thermal IR window to derive the bulk (mean) optical dust properties using the following expressions:

$$\langle \beta_e \rangle = \sum_{i=\lambda_1}^{\lambda_2} \left\{ \sum_{j=a1}^{a2} \left[\sum_{k=1}^{N} \omega_k(a_o) \sigma_e(a_o)_j \right] n(a_o)_j \Delta a_o \right\} \quad (1)$$

$$\langle \beta_s \rangle = \sum_{i=\lambda_1}^{\lambda_2} \left\{ \sum_{j=a1}^{a2} \left[\sum_{k=1}^{N} \omega_k(a_o) \sigma_e(a_o)_j \right] n(a_o)_j \Delta a_o \right\} \quad (2)$$

$$\langle \varpi \rangle = \frac{\langle \beta_s \rangle}{\langle \beta_e \rangle} \quad (3)$$

$$\langle g \rangle = \frac{\sum_{i=\lambda_1}^{\lambda_2} \left\{ \sum_{j=a1}^{a2} \left[\sum_{k=1}^{N} \omega_k(a_o) g(a_o)_j \sigma_s(a_o)_k \right] n(a_o)_j \Delta a_o \right\}}{\langle \beta_s \rangle} \quad (4)$$

where $\langle \beta_e \rangle$, $\langle \beta_s \rangle$, $\langle \varpi \rangle$, and $\langle g \rangle$, all functions of wavelength, are the bulk mean extinction and scattering coefficients, single-scattering albedo, and mean asymmetry parameter, respectively. Particle extinction and scattering cross sections are denoted as σ_e and σ_s, respectively. In equations (1), (2), and (4), the first summation from λ_1 to λ_2 is over the wavelength spectral domain, while the second summation from a_1 to a_2 is over the APS size intervals [n (a_o)], where n is particle count per cm^3 evaluated at the center of each APS size bin a_o (μm). The third summation from 1 to N is over the shape distribution for N possible dust shapes with ω (a_o) being the aspect ratio weighting factor. It is noted that the size integration of optical properties for the oblate spheroid was performed over size bins ranging from 0.1 to 5 μm in steps of 0.2 μm. Because of the large memory requirements and computational time required by FDTD, the size integration for the compact hexagon was performed over three size bins from 0.1 to 2.5 μm (Table 1).

[17] Figures 2a and 2b show the calculated single-scattering albedos (ϖ) and asymmetry parameters (g) for pure and internally mixed mineral compositions employing the T-matrix and FDTD methods over the window region. Oblate spheroids and compact hexagons are labeled (OS) and (CH), respectively. Four mineral compositions are shown, including the Volz model (V), 100% quartz (Q), kaolinite/10% hematite mixture (K/H) and a kaolinite/50% calcium carbonate mixture (K/C). Pure kaolinite (not shown) has similar values as compared to the mixtures. Figures 2c and 2d show the corresponding size variation for the Volz ϖ and g, respectively. The single-scattering properties show little change with size as compared to mineral composition, although some slight differences are noted. For example, Figure 2c shows that as particle size increases, so too does ϖ ($\leq$4%), due possibly to an increase in particle

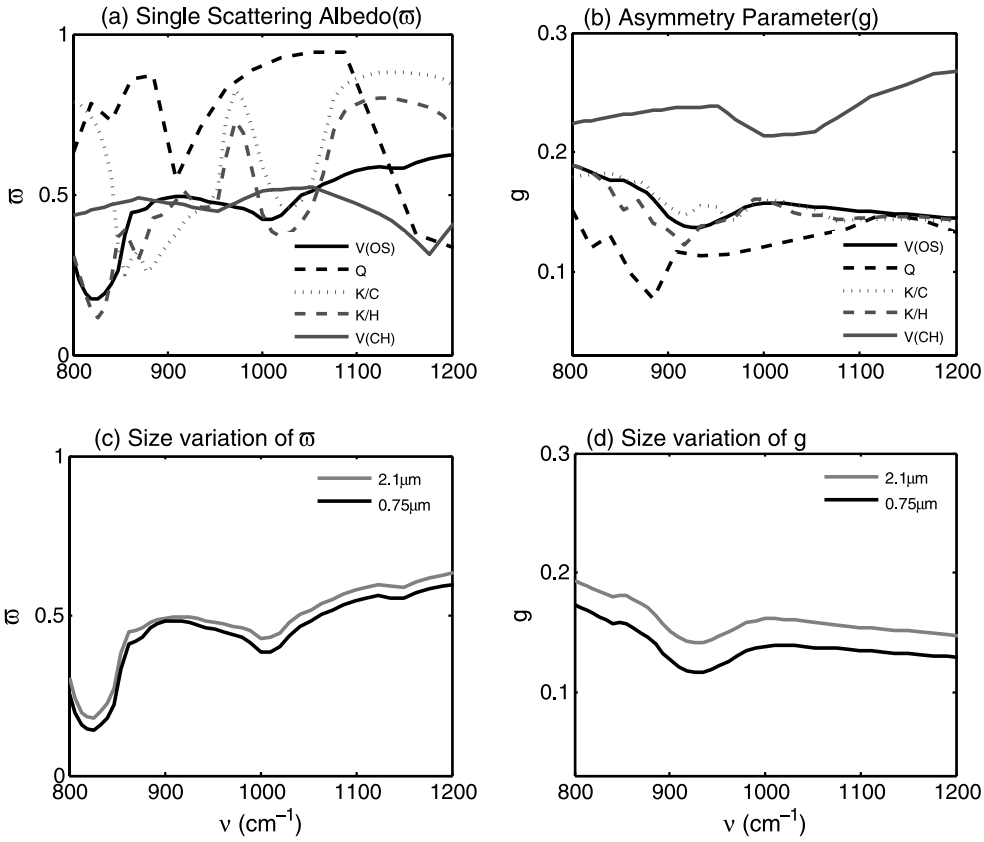

Figure 2. Dust single scattering properties for compact hexagons (CH) and oblate spheroids (OS) with variable compositions in the thermal IR window. (a) Single scattering albedo for four compositions. (b) Asymmetry parameter for the same dust parameters. (c) Volz size variation of single scattering albedo. (d) Same as Figure 2c but for asymmetry parameter.

surface area. Radiative transfer simulations show that increased scattering reduces the magnitude of the emissivity effects of the resulting BT spectrum when observed from a ground-based AERI system. The spectral average and the root mean square (RMS) variance of ϖ and g are 0.4629 ± 0.0231 and 0.1563 ± 0.0162, respectively. In Figures 2a and 2b, we note the complex spectral variability in the optical properties of each composition. For comparison, the solid black curves represent the FDTD optical parameters for the Volz compact hexagon with an effective size distribution $r_{eff} = 2$ μm. Consistent with *Highwood et al.* [2003], our single-scattering properties for the cases analyzed exhibit greater spectral variability with refractive index compared to particle size or shape. This illustrates the significance of having a priori knowledge of particle composition for accurately retrieving dust properties. It further demonstrates the ability of using AERI spectra for retrieving the mineral composition of airborne dust.

[18] In Figure 2a, the compact hexagons in the 8–9 μm spectral region scatter more (by about a factor of 2) than oblate spheroids. In the intermediate part of the window region, both shapes have similar single-scattering albedos, whereas in the 11–12 μm region, the hexagonal particles exhibit greater absorption. These differences may be attributed to the reduced size integration for the compact hexagon, where contributions from larger sized particles were not considered. Differences may also be caused by the integration over particle shape for the oblate spheroid since we only considered a single shape using FDTD. In Figure 2b, the compact hexagons are shown to have a significantly greater amount of forward scatter than do oblate spheroids. It is noted that the asymmetry parameter for FDTD is scaled down 3 times for comparison. Generally, the asymmetry parameter for each composition is found to decrease with wave number.

2.4. Radiative Transfer Model

[19] We used the Code for High-resolution Accelerated Radiative Transfer with Scattering (CHARTS [*Moncet and Clough*, 1997]) for simulating the downwelling AERI radiances. CHARTS employs the adding-doubling method for aerosol and cloud scattering, coupled with a line-by-line radiative transfer model (LBLRTM [*Clough et al.*, 1992]) having a line resolution ($\Delta\nu$) of 0.00015 cm^{-1}, for calculating gaseous absorption/transmission using the HITRAN-2000 line parameter database [*Rothman et al.*, 1992]. This radiative transfer code also includes the CKD2.4 water vapor continuum model developed by *Clough et al.* [1989]. The dust parameters shown in Figure 2 were incorporated into CHARTS along with the dust scattering and absorption coefficients for calculating the AERI spectral radiances, which were subsequently converted into equivalent BT spectra. Model calculations were carried out from level 1 (surface), while the viewing zenith angle

was defined to be at 0° with respect to the local zenith. To adequately represent the regional atmospheric state, the temperature and relative humidity profiles employed in the model atmospheres were taken from MAARCO and Abu Dhabi airport radiosondes and covered over 43 vertical layers with a grid spacing of 1 km. The bottom boundary was characterized by an averaged spectral emissivity over the window region corresponding to a dark brown quartz surface. Assuming that the lowest dust layer is adjacent to the surface (i.e., near the source), the transfer of IR radiation in a dust-laden atmosphere can be partitioned into three components involving emissions by the dust layer(s), transmitted clear-sky emissions mainly from water vapor, and reflections of the surface emissions by dust layer(s). The downward IR radiance reaching the surface can then be expressed by

$$I\downarrow = \int_{p_{top}}^{p_{sur}} B[T(p')]\frac{d\Im_{dust}(p-p')}{dp'}dp' + \Im_{clr}\Im_{dust}\left(\int_{p_0}^{p_{top}} B[T(p')]\frac{d\Im_{clr}(p-p')}{dp'}dp' + r(\Im_{dust})\left[B(T_{sur})\Im_{dust} + \int_{p_{top}}^{p_{sur}} B[T(p')]\frac{d\Im_{dust}[p-p']}{dp'}dp'\right]\right) \quad (5)$$

where $I\downarrow$ is the downward surface radiance, $B[T]$ is the Planck radiance, and $\Im_{clr}$ and $\Im_{dust}$ are the transmitted radiances for both clear and dust layers, respectively. The variables p_{sur}, p_{top} and p_0 represent the surface pressure, pressure at the top of the dust layer(s) and pressure at the top of the atmosphere, respectively. Last, r is the reflectance from both the surface and the dust layer(s), which is negligible compared with the emission terms since the dust is at the surface. Note that the longwave scattering effects of mineral aerosols have been previously investigated by *Dufresne et al.* [2002]. The wave number (ν) dependency of all the variables is implied in equation (5). The model dust layers range from the surface up to a maximum of 5 km, consistent with most field observations and the dust properties are prescribed to be uniform and homogeneous inside each layer.

3. Sensitivity Studies: Pristine and Dust-Laden Atmospheres

[20] Simulations were performed to evaluate the sensitivity of the AERI surface BT spectra to a number of critical dust and atmospheric parameters over the thermal IR window. First, we evaluate the AERI spectral response to changes in precipitable water vapor (PWV) as a potential constraint in the methodology. Second, the effect of the vertical distribution of water vapor and temperature on AERI clear-sky spectra is investigated for cloud and dust-free atmospheres. Third, the spectral response to various dust-cloud scene scenarios for developing an AERI detection algorithm is examined. Fourth, the sensitivity of AERI spectra to key dust parameters including particle size and shape, optical depth and dust cloud altitude and thickness are evaluated. Fifth, an estimated radiance error spectrum is constructed corresponding to the nonlinear response of the MgCdTe detector which is used for testing the sensitivity of the dust detection/retrieval methodology (results are presented in section 4). Last, the model atmosphere and clear-sky spectra employed in this study are presented.

Table 2. AERI Subbands

Subband Index	ν (cm^{-1})	λ (μm)
1	809.0–812.9	12.30
2	815.3–824.5	12.10
3	828.3–834.6	12.00
4	842.8–848.1	11.80
5	860.1–864.0	11.60
6	872.2–877.5	11.43
7	891.9–895.8	11.16
8	898.3–905.5	11.08
9	929.6–939.7	10.60
10	959.9–964.3	10.39
11	985.1–998.1	10.00
12	1076.7–1084.9	9.25
13	1095.0–1098.2	9.12
14	1113.5–1116.1	8.97
15	1124.4–1132.6	8.86
16	1142.2–1148.0	8.73
17	1155.3–1163.5	8.63

3.1. Sensitivity of BT to Water Vapor and Temperature

[21] The thermal IR window is a relatively "clean" spectral region, useful for retrieving aerosol and cloud properties [*Turner et al.*, 2003; *Deslover et al.*, 1999; *Pierangelo et al.*, 2004, 2005; *DeSouza-Machado et al.*, 2006]. With the selection of narrow "subbands" [*Deslover et al.*, 1999] inside the window region (see Table 2 for subband locations), the effects of line absorption by water vapor and other trace gases are further minimized. However, absorption due to water vapor continuum remains to be a source for error in IR remote sensing applications. Previous studies of the affects of water vapor in the IR have included *Realmuto and Worden* [2000], *Kumar et al.* [2003], *Kahn et al.* [2005], and *Moy et al.* [2005], to name a few. *Moy et al.* [2005] in particular, conducted an AERI noise analysis, including instrumentation and water vapor uncertainties and showed that the water vapor error clearly dominates the AERI signal in the 10 μm region. Accounting for the dynamic effects of water vapor is therefore critical for IR remote sensing applications.

3.1.1. Sensitivity of BT to PWV

[22] To test the sensitivity of the clear-sky spectra to changes in total column water vapor amount, radiative transfer simulations using CHARTS were performed on the basis of the scaled water vapor profiles from averaged MAARCO radiosonde data during September 2004 for a range of PWV consistent with AERONET measurements ($\sim$1.5–4 gcm^{-2}). Profiles were averaged to represent the mean atmospheric state during this relatively active dust period. Figure 3 shows the sensitivity of the AERI BT spectra at each subband (denoted by the markers) to changes in total column water vapor inside the window region. The curves roughly corresponding to the minimum, maximum and average PWV profiles during the UAE^2 are labeled 1.57, 3.96 and 2.43 g cm^{-2}, respectively. The plot reveals that the sensitivity is strongly dependent on wave number, where large changes in BT are more evident in the shorter wave number regions (i.e., 800–900 cm^{-1}) because of

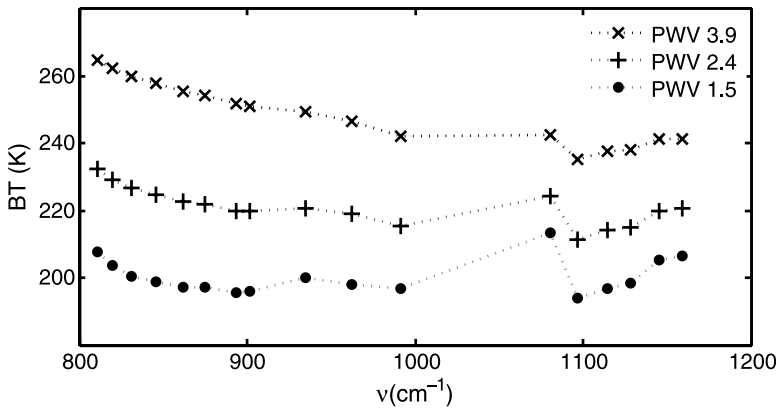

Figure 3. Sensitivity of AERI "clear-sky" subband spectra to changes in PWV (g cm^{-2}). Markers denote subband locations.

larger water vapor continuum absorption coefficients [*Grant*, 1990].

[23] Observed changes in the retrieved PWV derived from the 0.94 μm channel of the AERONET Sun photometer [*Bruegge et al.*, 1992] can vary as much as 15–30% in as short as several hours. Such changes over short time scales could underestimate or overestimate the effects of dust if not properly accounted for in the detection/retrieval scheme. For example, an 18% increase in PWV from 2.8 to 3.3 g cm^{-2}, will increase the average clear-sky BT spectra by ~3.9% or 9.3 K, around the same order of magnitude as dust [e.g., *Highwood et al.*, 2003]. Furthermore, a ±10% uncertainty in the PWV retrieval [*Bruegge et al.*, 1992] for the range of PWV considered in this study translates to an uncertainty in the averaged clear-sky BT spectra of about ±4–6 K. On the basis of radiative transfer calculations, this uncertainty corresponds to an IR optical depth (τ) of ~0.075 at 962 cm^{-1} or ~0.15 at 0.55 μm using a Volz extinction coefficient ratio for 1 μm sized dust particles.

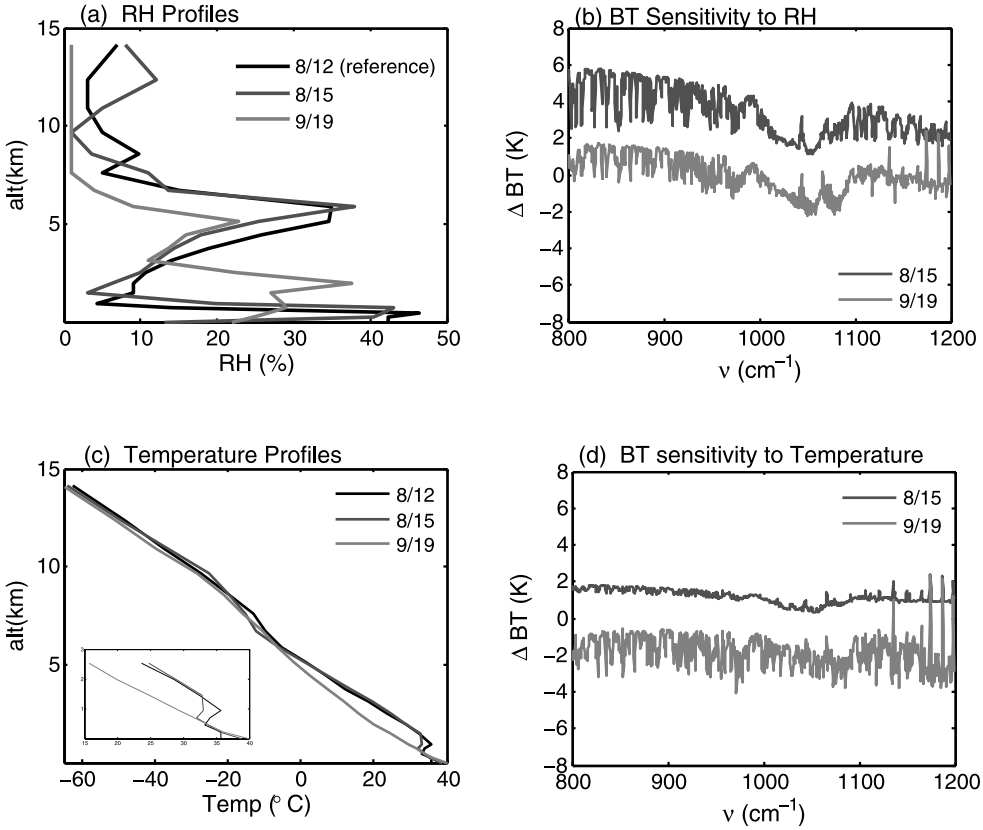

Figure 4. Sensitivity of AERI BT spectra to changing RH and temperature profiles for 3 days during UAE^2. (a) RH profiles with the same PWV (~2.3 g cm^{-2}). (b) BT sensitivity to RH (ΔBT = profile − reference spectrum). (c) Temperature profiles for same days. Inset shows profiles inside PBL. (d) BT sensitivity to temperature.

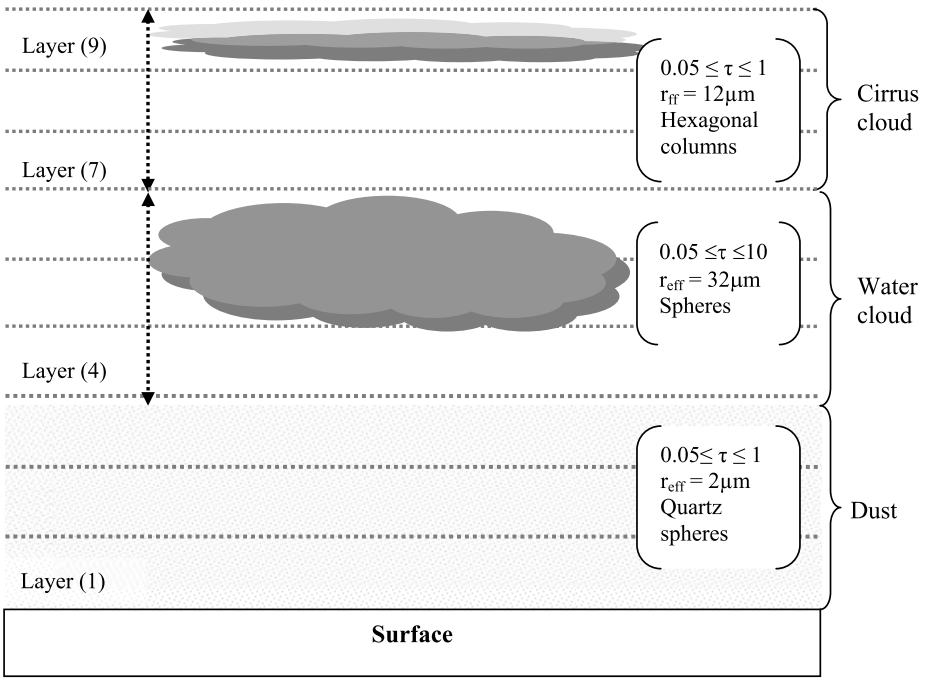

Figure 5. Positions and properties of dust/cloud layers used in model simulations for AERI detection. Double-sided arrows represent the altitude range of cloud layers evaluated.

[24] To minimize bias, a look up table (LUT) of PWV and BT spectra can be constructed to remove the continuum effects of water vapor (i.e., a clear-sky correction) from spectral measurements. This is further discussed in sections 4 and 5 in connection with AERI dust detection. Last, there is also uncertainty in the vertical distribution of water vapor having the same PWV. Sensitivity of the BT spectra to this and uncertainty in the vertical temperature distribution are discussed in the following.

3.1.2. Sensitivity of BT to Water Vapor and Temperature Vertical Distributions

[25] UAE^2 radiosonde data from Abu Dhabi Airport were analyzed to examine the sensitivity of AERI BT spectra to variable water vapor distributions having the same PWV (2.3 ± 0.01 g cm^{-2}). Figure 4a shows the relative humidity (RH) profiles for 3 days (12 and 15 August and 19 September) where water vapor peaks near the surface. The BT spectrum for each case was computed and differenced with an arbitrarily chosen reference spectrum (ΔBT, 12 August due to its smaller BTs) to plot the relative differences. Figure 4b shows the sensitivity of 2 days (15 August and 19 September) with respect to the reference spectrum. Given the selected water vapor distributions, the three cases in terms of their mean differences over the window region were within ~0.005 to 3.37 K of each other. For a fourth case analyzed (not shown), the mean spectral difference was about 8 K because of a peak shift in water vapor from the surface to a height of nearly 5 km, attributed likely to a passing dust storm.

[26] Using the same sounding data, a similar analysis was conducted by evaluating the BT sensitivity to changes in the vertical temperature profiles while holding water vapor constant. Figures 4c and 4d show the temperature profiles and relative BT differences between the same 3 days, respectively. The variability of temperature inside the boundary layer is shown in the inset to Figure 4c, where a maximum difference of ~8°C is evident. For these cases, the relative BT differences were within ~1.18 to 3.0 K of each other. Similarly for the fourth case analyzed, a maximum difference of ~6 K was observed.

3.2. Sensitivity of BT for Cloud/Dust Discrimination

[27] Subbands that are most sensitive to clouds or dust were selected for developing a dust detection algorithm using AERI spectral radiances. A description of the cloud and dust models follows with the specified parameters adequately representing the observed dust/cloud conditions during the UAE^2.

3.2.1. Cloud and Dust Model Descriptions

[28] The FDTD IR database [*Yang et al.*, 2005] was used to model the cirrus cloud optical properties where ice crystals were assumed to be hexagonal columns with an effective size of 12 μm based on the size distribution data collected by the Cloud, Aerosol, and Precipitation Spectrometer (CAPS) aboard the WB-57 aircraft during CRYSTAL-FACE. Using UAE^2 MPL data to identify cirrus cloud positions, the model cirrus cloud top heights were located between 7 and 9 km with geometrical thicknesses ranging from 1 to 2 km. Cirrus cloud optical depths (COD) were varied from 0.05 to 3, however, we mainly focused on the BT effects of thin cirrus ($\tau_c \leq 1$) having spectra very similar to dust. Liquid water clouds were assumed to be composed of spherical particles with a monodispersed droplet radius of 32 μm. On the basis of UAE^2 MPL data, the water cloud base heights were positioned between 3 and 4 km with a geometrical thickness of 2 km. Water COD (τ_w) was varied from 0.05 to 10 in the sensitivity study.

[29] The model dust layers consisted of four mineralogical compositions: Volz (V), quartz (Q), kaolinite (K), and kaolinite carbonate (K/C) mixture. Dust particle shape and

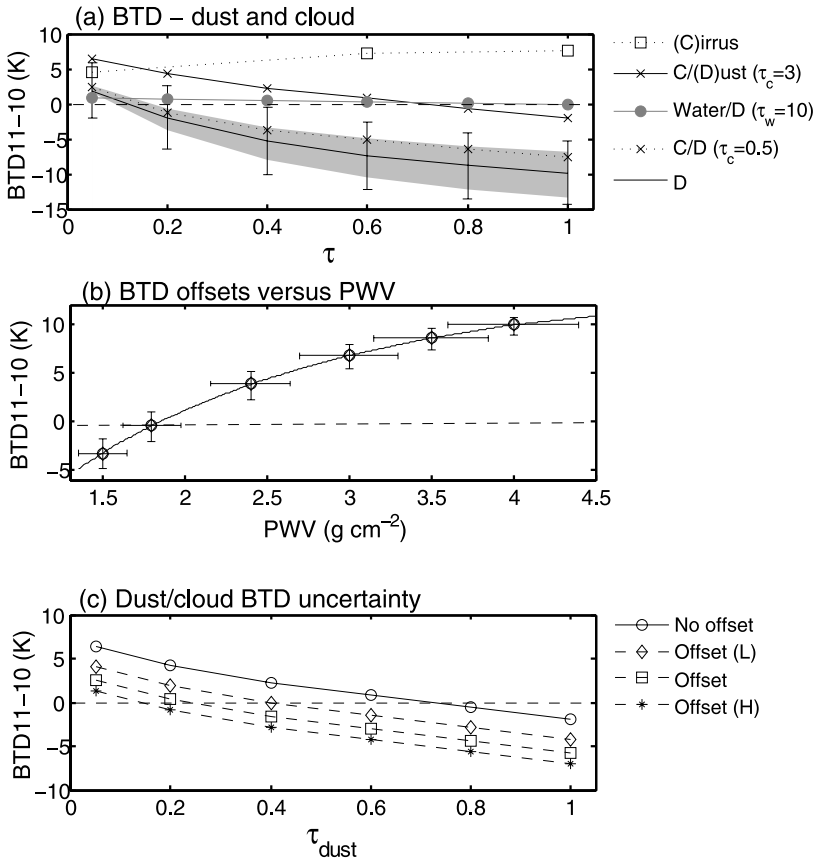

Figure 6. (a) BTD 11–10 versus optical depth for dust (Q) and cloud conditions. Shown are the cirrus (C)/dust (D) only and mixed cloud/dust scenarios including liquid water cloud (W). (b) BTD clear-sky correction uncertainty versus PWV. (c) Dust and cloud with BTD corrections applied. L/H represents the low/high ends of PWV uncertainty. See text for details.

size distributions were characterized by the parameters defined in section 2. The dust was uniformly distributed within the lowest 3 km in all scenarios with dust optical depths (τ_d) ranging from 0.05 to 1.0. The model dust and cloud layers are illustrated in Figure 5.

3.2.2. Model Simulations

[30] Theoretical calculations were performed for a number of possible dust/cloud scenarios: (1) dust (D) only, (2) cirrus cloud (C) only, (3) cirrus cloud with dust (C/D), and (4) liquid water cloud with dust (W/D). The model results for all scenarios are presented in Figure 6a. The dust only and mixed optically thin cirrus (τ_c = 0.5) and dust cases (solid black curve and dotted black curve with crosses, respectively) show a common trend in the BT slope from λ = 10 μm (subband 11) to λ = 11.16 μm (subband 7), herein referred to as a BTD 11–10. For simplicity, the dust model results are given in terms of spherical quartz particles with a r_{eff} of 2 μm. Since most minerals with the exception of pure calcium carbonate tend to absorb more at wavelengths near 10 μm than at 11.16 μm (Figure 1), their BTD 11–10 are negative. This behavior is similar to that of the slope of MODIS BTD 8–11 versus BTD 11–12 which is used by *Hansell et al.* [2007] for distinguishing dust from cloud.

[31] The results for scenarios 1 (dust only, i.e., τ_c/τ_w = 0) and 2 (cirrus only, i.e., τ_d = 0) are presented in Figure 6a where the BTD 11–10 is plotted as a function of optical depth (τ). The shaded gray region around the dust only curve represents the variability in the BTD 11–10 as particle size changes where the lower, center and upper bounds of the region represent particles having sizes 0.75, 2 and 5 μm, respectively. Likewise, the error bars on the dust only curve represent the variability in BTD 11–10 due to a 25% uncertainty in PWV (2.4 g cm^{-2} is the mean, and 1.8 and 3.0 g cm^{-2} are the extrema). Clearly the variability in BTD 11–10 due to the uncertainty in PWV exceeds that due to particle size. As both particle size and PWV increase, so too does the BTD 11–10, which may cause the detection of clouds to be overestimated. Likewise, the BTD slope for water vapor when PWV $\leq$ 1.84 g cm^{-2} is similar to mineral dust which may cause dust to be overestimated. For optical depths greater than 0.12, dust has a negative BTD 11–10, whereas when dust is optically thin ($\tau_d \leq 0.12$), the effects of water vapor dominate and the BTD 11–10 becomes positive. The cirrus only case on the other hand displays a positive BTD 11–10 since ice water absorbs more strongly with longer wavelengths. Note the zero-point threshold (BTD 11–10 = 0) is given by the dashed black line.

[32] Two mixed dust/cirrus cases are presented to describe the effect on BTD 11–10 when the cloud optical depth (τ_c) increases from 0.5 to 3 (dotted and solid black curves with crosses, respectively). When cloud and dust are optically thin, the effects of water vapor dominate and the BTD 11–10 is positive. As dust optical depth increases under a thin cirrus cloud, the BTD 11–10 becomes increas-

Table 3. Summary of BT Sensitivity for Dust/Cloud Detection[a]

	Cloud			Altitude (km)		
Mineral	Phase	COD	PWV (g cm^{-2})	Dust	Cloud	BTD 11–10 (K)[b]
Q	NC	-	2.4	1–3	-	−5.48 ± 2.22
Q	NC	-	1.8	1–3	-	−11.37 ± 2.02
Q	NC	-	3.0	1–3	-	−1.84 ± 1.38
V	NC	-	2.4	1–3	-	−6.00 ± 2.27
K	NC	-	2.4	1–3	-	−3.87 ± 2.03
K/C	NC	-	2.4	1–3	-	−4.84 ± 1.67
ND	I	-	2.4	-	9	6.43 ± 1.72
ND	W	-	2.4	-	3–4	1.41 ± 0.71
V	I	0.05	2.4	1–3	9	−2.13 ± 3.31
V	I	0.05	2.4	1–3	7–8	−1.92 ± 3.32
V	I	3.00	1.8	1–3	7–8	2.41 ± 2.47
V	I	3.00	1.8	1–3	9	0.70 ± 3.14
V	I	3.00	3.0	1–3	7–8	4.42 ± 2.37
V	I	3.00	3.0	1–3	9	4.01 ± 3.03
V	W	10.00	1.8	1–2	3–4	0.38 ± 0.23
V	W	10.00	2.4	1–2	3–4	0.61 ± 0.24
V	W	10.00	3.0	1–2	3–4	0.84 ± 0.25
V	W	10.00	2.4	1–2	5–6	0.61 ± 0.24
V	W	1.00	2.4	1–2	3–4	−1.45 ± 1.22

[a]Mineral nomenclature: Q, quartz; V, Volz; K, Kaolinite; KC, Kaolinite/Carbonate; ND, no dust; NC, no cloud; I, ice cloud; W, water cloud; COD, cloud optical depth.

[b]BTD 11–10 is calculated as an average quantity plus 1 standard deviation (1σ) over the respective particle sizes and optical depths (refer to text for discussion).

ingly negative (dotted black). When cirrus cloud optical depth increases (solid black) or as the height of the cirrus cloud is reduced (e.g., from 9 to 7 km), the BTD 11–10 becomes more positive which makes it more difficult to detect dust even when dust optical depths are high. Figure 6a, for example, shows that under an optically thin cirrus cloud, dust would require a minimum optical depth threshold (τ = 0.12) to be detected. If the COD were to increase, the threshold for detecting dust would be well over 0.6. Similar analysis employing satellite data for mixed aerosol and cirrus cases, including dust, was performed by *Roskovensky et al.* [2004], *Roskovensky and Liou* [2005], and *Hansell et al.* [2007].

[33] Figure 6a also shows an example of dust and water cloud (gray curve with solid circles) with a τ_w of 10. The BTD 11–10 is positive for all dust optical depths; that is, the dust will not be detected. This same result occurred when the layers of water cloud and dust were reversed (e.g., in a transported dust plume). Not shown is the case for a thin water cloud (τ = 1), where BTD 11–10 is negative for dust optical depths greater than 0.05. Last, the sensitivity to cloud height was evaluated by elevating the water cloud to 5–6 km. No significant change in the BTD 11–10 was observed; hence the main variable controlling the BTD 11–10 behavior of water cloud with dust is the COD. A summary of the results presented is given in Table 3.

[34] Last, sensitivity of the BTD 11–10 to dust particle asphericity was evaluated by comparing the spherical case to a shape distribution of oblate spheroids (section 2). Over the range of optical depths (0.05–1.0), the mean absolute difference was found to be ~4 K with a tendency to shift the BTD 11–10 more negative.

3.3. Sensitivity of BT to Dust Parameters

3.3.1. Particle Size and Shape

[35] To assess the sensitivity of the AERI BT spectra to dust particle size and shape, we examined spheres (S), oblate spheroids (OS) and compact hexagons (CH) each having a lognormal size distribution with an effective radius that is increased from 0.5 to 2.0 μm in steps of 0.5 μm. Dust composition was prescribed using the *Volz* [1973] refractive indices. For each size step, dust optical depths were adjusted to 0.05, 0.4 and 1.0 to assess both optically thin and thick dust layers. The sensitivity results shown in Figures 7a and 7b are expressed as a function of both effective size and shape and are plotted in terms of their BTD slope across the upper (BTD 17–13) and lower (BTD 11–1) subbands, respectively. To illustrate differences between each parameter, the sphere and compact hexagon results were compared over the specified size range at an optical depth of 0.4.

[36] Comparing Figure 7a with Figure 7b shows that particle shape sensitivity appears to be greater across the upper subbands (USB), while particle size sensitivity is greater across the lower subbands (LSB). For example, the BTD between sphere and compact hexagon shown in Figure 7a varies from 4 to 8 K over the given particle size range, whereas in Figure 7b, the same BTD varies only from 0.3 to 2 K. Likewise, although the BTDs between particle sizes are much greater for submicron particles, particularly compact hexagon, variations are less than 0.5 K across the USB to between 0.5 and 1.5 K across the LSB. It is also interesting to point out that as the effective size increases, the BTD slope increases/decreases for the USB/LSB regions, respectively.

[37] The BTD sensitivity for both parameters was also found to increase with dust optical depth and for particles having effective radii less than or equal to 1 μm. An increase in optical depth from 0.05 to 1, for example, produces a fivefold increase in the BTD size sensitivity in the LSB region for a 1 μm sized compact hexagon. For the geometries and sizes considered, similar changes in the BTD shape sensitivity were also noted although these changes were generally found to be greater in magnitude

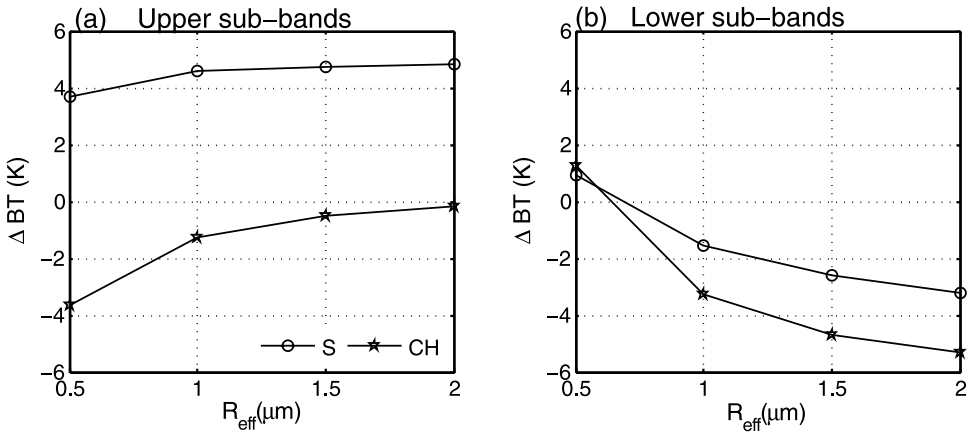

Figure 7. Particle size and shape BT sensitivity across (a) upper subbands (USB: 13–17) and (b) lower subbands (LSB: 1–11). Shown are spheres (S) and compact hexagons (CH) with an effective size range of 0.5–2 μm. Dust optical depth is fixed at 0.4.

as compared to particle size. For example, the BTD size sensitivity for a compact hexagon when averaged over the size range is -1.36 ± 1.2 K. In comparison, the BTD shape sensitivity for a 0.5 μm sized particle when averaged over each shape is -6.19 ± 3.5 K.

3.3.2. Dust Optical Depth

[38] The theoretical basis for the optical depth retrieval method lays in the subband slope dependence of dust optical depth, particularly from 1100 to 1200 cm^{-1} which covers subbands 13–17. This spectral region is emphasized because of the higher BT sensitivity to PWV from 800 to 1000 cm^{-1} (Figure 3) and also the strong ozone absorption at 1086 cm^{-1}. Two cases are presented in Figure 8 to illustrate the slope sensitivity from subbands 13 to 17 by employing two dust microphysical models: Volz hexagonal plates and kaolinite/carbonate mixture of oblate spheroids. The curves are dust ΔBT spectra where ΔBT is defined as follows:

$$\Delta BT = BT_{dust} - BT_{clear} \tag{6}$$

where BT_{dust} and BT_{clear} represent the modeled or observed dust and clear-sky spectra respectively, across AERI subbands. To a first approximation, ΔBT over the window region can be used as a rough qualitative indicator of the dust IR forcing, since this is where most dust absorption occurs. The markers from left to right denote the subband locations 1–17. Dust optical depths were varied from 0.05 to 1.0 in increasing order from bottom to top. For both cases, AERI observed spectra (broken gray curves) are shown for comparison. Note the reasonable fit between subbands 13–17; however, larger differences occur particularly in the 800–900 cm^{-1} region, which can be attributed to water vapor and uncertainty in dust composition. Similar results were also found using other dust models.

[39] Figures 8a and 8b show a positive increase in the subband slope as optical depth becomes larger because of enhanced particle absorption at these wavelengths. The lines connecting subbands 13–17 (Figure 8a) illustrate the optical depth slope dependence. Also note the sharp spectral folding (Figure 8a) and the much smoother spectral roll-off (Figure 8b) near 1100 cm^{-1} for each dust model, respectively. This spectral behavior follows the imaginary terms of the refractive indices (Figure 1), which shows that most minerals exhibit peak absorption around 1000–1100 cm^{-1} with smaller secondary peaks scattered throughout the window region. As the absorption increases, so too does the spectral peak, which causes the slope to further increase.

3.3.3. Dust Altitude

[40] To assess the sensitivity of the AERI BT spectra to changes in dust altitude (Z), we took a homogeneous dust layer near the surface with a geometrical thickness of 1 km and progressively increased its altitude in 1 km increments until a layer height of 5 km was reached. This is analogous to dust being lifted and transported away from its source.

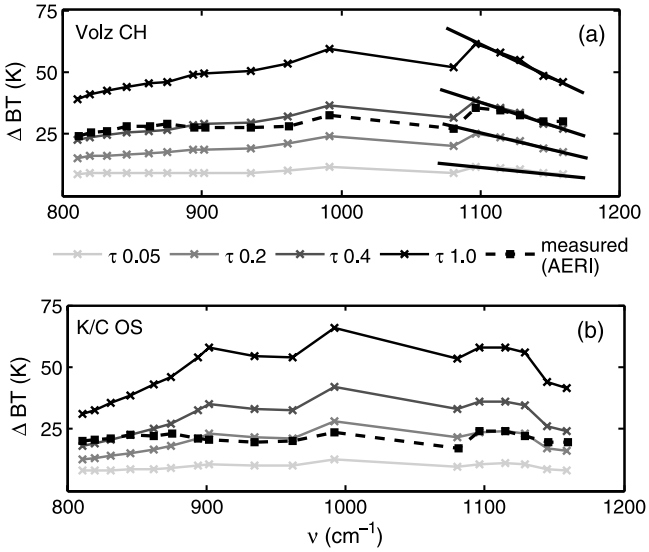

Figure 8. BT sensitivity to dust optical depth at 962 cm^{-1} with markers denoting locations of AERI subbands 1–17 from left to right. (a) Volz CH model spectra for four optical depths with best fit AERI spectrum. (b) Same as Figure 8a but for K/C OS dust model.

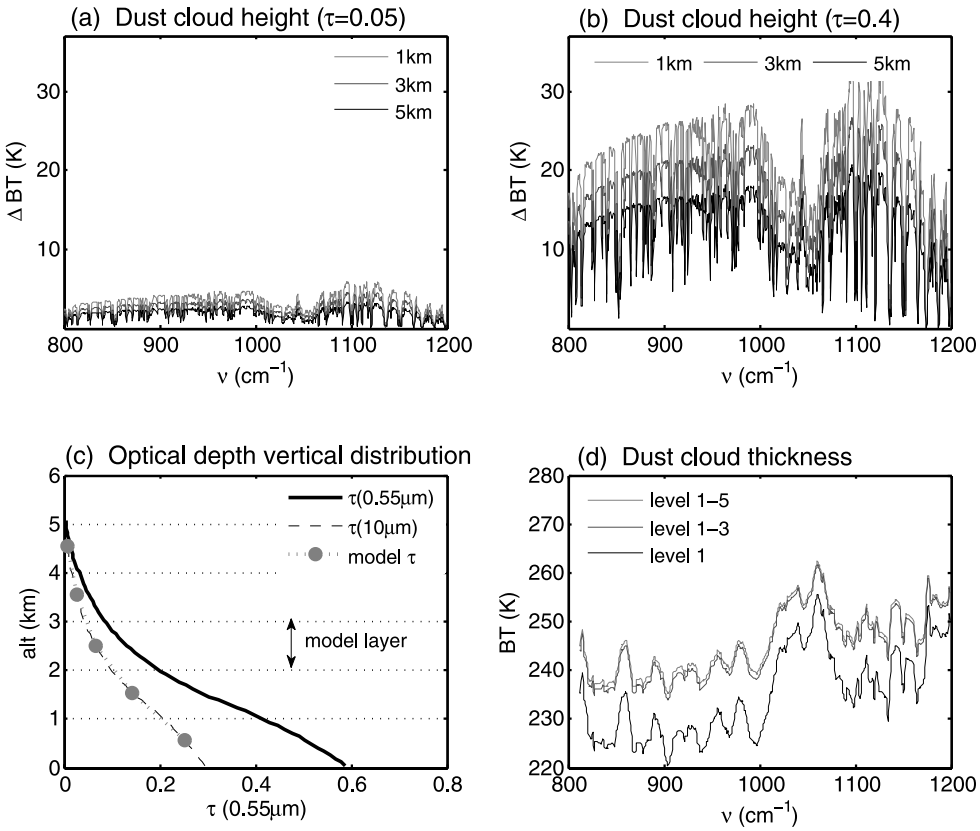

Figure 9. (a) BT sensitivity to dust cloud height for altitudes z = 1, 3, and 5 km at optical depth τ = 0.05. (b) Same as Figure 9a but for τ = 0.4. (c) MPL optical depth profile used to model optical depths for each layer. (d) BT sensitivity to dust cloud thickness.

The dust model consisted of spherical particles with a lognormal size distribution (r_{eff} = 2.0 μm; σ_{gv} = 2.0) and mineral composition defined by the Volz refractive indices. The resulting changes in BT for a given altitude change ($\Delta BT/\Delta Z$) at dust IR optical depths of 0.05 and 0.4 are presented in Figures 9a and 9b for altitudes of 1, 3, and 5 km. As the dust layer's altitude increases, the magnitude of the resulting BT spectrum decreases but is dependent on dust optical depth. Optically thin dust (τ_d = 0.05) having undergone an altitude change of 5 km, results in a relatively small BT decrease of ~1.8 K (Figure 9a). This means that AERI is not very sensitive to the altitude changes of light dust and the resulting error will be small. Increasing the optical depth to 0.4 (Figure 9b) for the same altitude change, however, results in a much larger BT decrease of up to 10 K because of enhanced dust absorption. This has significant implications for detecting/retrieving transported dust plumes such as in the case of dust inside the SAL.

3.3.4. Dust Thickness

[41] The effects of dust layer thickness (ΔZ) on AERI surface spectra are examined by successively incrementing the number of dust layers used during each simulation. Beginning with the first dust layer near the surface, additional layers are added until the geometrical thickness of the dust cloud reaches 5 km. This range in dust thickness is consistent with observations during the UAE^2 where dust top heights were often capped by a strong inversion around 5 km. The dust properties were assumed to be uniform and homogeneous across each layer. Dust particle shape and size were characterized by spheres with a lognormal size distribution of r_{eff} = 2 μm and σ_{gv} = 2. A vertical distribution of dust optical depths from the UAE^2 level 1.5a MPLNET [*Welton et al.*, 2001] data set on 22 September 2004 was used (Figure 9c). The black and gray curves denote the MPL retrieved optical depth profiles at 0.55 and 10 μm, respectively, where the latter was obtained by scaling the visible optical depths using the Volz extinction coefficient ratio between 0.55 and 10 μm. The circles on the gray curve represent the scaled IR optical depths corresponding to the centers of each model dust layer. The BT spectra for a 1, 3 and 5 km thick dust cloud are shown in Figure 9d. A fivefold increase in layer thickness (from 1 to 5 km) can result in a positive increase of the averaged AERI spectra of ~10 K over the window region. This represents the maximum error using the assumed optical depth profile. Uncertainty in dust thickness at higher altitudes (e.g., from 3 to 5 km) where dust optical depths are reduced would result in errors in the range of 2–5 K. As more layers are added, the relative difference between each resulting spectrum decreases. Level 1 denotes a one-layer-thick dust cloud; Level 1–3 denotes a three-layer-thick dust cloud etc. Refer to Table 4 for a summary of the BT sensitivity for the dust and atmospheric parameters presented.

3.4. AERI MgCdTe Detector Nonlinearity

[42] The estimated radiance errors due to the MgCdTe detector nonlinearity were based on the prior works of

Table 4. Summary of BT Sensitivity to Dust and Atmospheric Parameters

Parameters	ΔBT Uncertainty (K)	Comments
Atmospheric		
PWV[a]	±4.00–6.00	
Water vapor variability[b]	±0.005–3.37	
Temperature variability[b]	±1.180–3.00	
Dust		
Particle size[c]		fix shape and vary sizes (0.05, 1.0, 1.5, 2.0 μm) at τ_d = 1
Compact hexagon (CH)	2.81 ± 2.61	
Oblate spheroid (OS)	−0.46 ± 0.17	
Sphere (S)	2.071 ± 1.37	
Particle shape[d]		fix size and vary shapes (CH, OS, S) at τ_d = 1
R_{eff} = 0.5 μm	−6.19 ± 3.50	
R_{eff} = 1.0 μm	−5.08 ± 2.40	
R_{eff} = 1.5 μm	−4.60 ± 2.10	
R_{eff} = 2.0 μm	−4.38 ± 1.90	
Optical depth[e]		COMPACT hexagon (Volz)
τ_d = 0.05	3.86 ± 0.184	
τ_d = 0.2	4.48 ± 0.566	
τ_d = 0.6	5.56 ± 1.017	
τ_d = 1.0	6.02 ± 1.133	
Altitude[f] (Z) (relative to level 1 at 1 km)		(−) sign → BT decrease
Level 1 to 2 (2 km)	−1.63 ± 1.07	
Level 1 to 3 (3 km)	−2.95 ± 1.97	
Level 1 to 4 (4 km)	−4.35 ± 2.94	
Level 1 to 5 (5 km)	−5.65 ± 3.86	
Thickness[g] (ΔZ) (relative to one layer)		(+) sign → BT increase
Two layers	8.70 ± 5.15	
Three layers	14.64 ± 8.13	
Four layers	18.81 ± 9.86	
Five layers	21.19 ± 11.84	

[a]Constrained by ±10% error in AERONET retrieved PWV during the UAE^2.
[b]Soundings from Abu Dhabi Airport having same PWV were used ((±0.01 g cm^{-2}).
[c]ΔBT is averaged over the size range across the lower subbands.
[d]ΔBT is averaged over the shape range across the upper subbands.
[e]ΔBT is averaged over particle size range 0.75–5 μm for upper subbands.
[f]ΔBTs averaged over dust optical depths τ_d = 0.05, 0.2 and 0.4. Altitude measured from level of dust top height for a 1 km thick dust cloud.
[g]ΔBTs averaged over dust optical depths τ_d = 0.05, 0.2 and 0.4. Thickness measured relative to a 1 km thick dust cloud.

Turner et al. [2004] and *Knuteson et al.* [2004]. The former authors studied the impact of the AERI MgCdTe detector nonlinearity on observed radiance spectra by using the corrections discussed by *Knuteson et al.* [2004]. The study found that the detector error was largest in clear-sky conditions for radiometrically cold scenes where the nonlinear response in the detector's electronics causes underestimation of the observed radiances. The effect is most evident in the window region, where the radiance residuals are in the approximate range of ~0.3–0.75 RU (1 RU = mW m^{-2} sr^{-1} cm^{-1}). Radiance residuals given by *Turner et al.* [2004] and *Knuteson et al.* [2004] were used to construct an estimated radiance correction spectrum over the thermal IR window with random noise added to account for the underestimated signal. Figure 10a shows the estimated nonlinearity corrections. Although the corrections are not exact, they provide a sense as to their potential effect on the detection/retrieval methodology. Details of the results are given in section 4.

3.5. Model Atmosphere and Clear-Sky Spectra

[43] To account for the temporal variability of the thermodynamic state parameters in the column atmosphere (i.e., temperature, relative humidity, etc), we combined the retrieved temperature and moisture profiles from the UW-SSEC AERIPLUS physical retrieval algorithm [*Feltz et al.*, 2003] for the planetary boundary layer (PBL) with regional sounding data using MAARCO radiosondes up to a height of 18 km. The AERIPLUS retrievals using only AERI data are limited below 2.5–3 km since most of the IR signal detected at the surface comes from the lower atmospheric emissions [*Feltz et al.*, 2003]. Because the AERI instrument measures near-surface emission precisely, the AERIPLUS retrieved parameters well represent the atmospheric state of the PBL.

[44] Figures 10b and 10c show the AERIPLUS retrieved time-height temperature and water vapor mixing ratio (WVMR) profiles for 22 September 2004 during the UAE^2. Temperature bias with and without the estimated MgCdTe error correction was 0.1°C, while that for WVMR was generally less than 0.5 g kg^{-1}, except the value at the surface of about 2 g kg^{-1}.

4. Dust Detection/Retrieval Methodologies and Case Studies

4.1. Detection Methodology

[45] Following the discussion in section 3, the AERI cloud/dust detection scheme employs the BTD 11–10 for separating cloud and dust using a dynamic threshold (BTD 11–10 = 0) where positive/negative BTD 11–10 is labeled as cloud/dust, respectively. Points near the zero-point threshold, i.e., within 0.1 K, are classified as uncertain. To compensate for water vapor in the algorithm and the

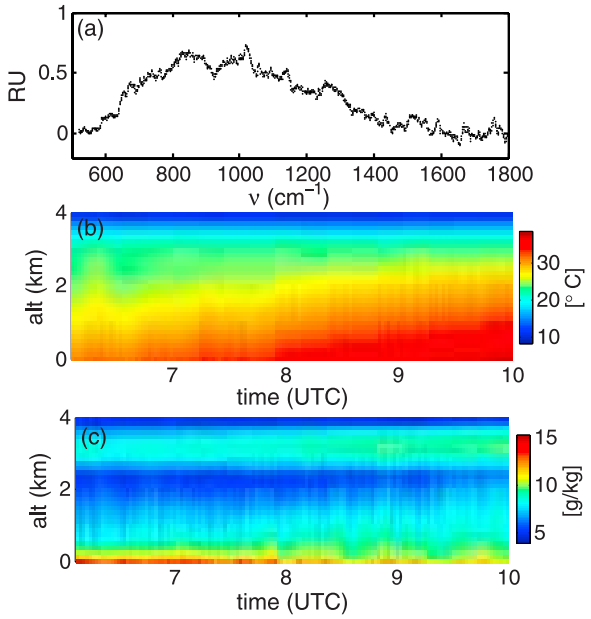

Figure 10. (a) Estimated radiance error (residuals) due to MgCdTe detector nonlinearity with vertical axis given in radiance units (1 RU = mW m^{-2} sr^{-1} (cm^{-1})). (b) AERIPLUS retrieved temperature profile from 22 September 2004 during UAE^2. (c) Same as Figure 10b but for WVMR.

potential for misclassifying dust, a BTD 11–10 clear-sky corrective term (offset), a function of PWV was introduced. The BTD correction was determined by comparing coincident measurements of AERONET derived PWV with AERI to a LUT which was calculated using the data from Figure 3 and then interpolated using a PWV spacing of 0.1 g cm^{-2}. For the cases examined and neglecting those dust episodes associated with strong weather systems (for example, haboob dust storms [see *Miller et al.*, 2008]), the water vapor uncertainty (total column and vertical variability) can produce averaged clear-sky BTD errors in the range of ~0.005–6 K with most error attributed to the total column. The sensitivity of the BTD 11–10 to water vapor vertical distribution with a constant PWV was found to be in the range of ~0.005–3.37 K. The effects of column water vapor uncertainty are shown in Figure 6b in terms of the BTD 11–10 clear-sky correction as a function of PWV. The horizontal error bars denote the ±10% PWV uncertainty in the AERONET measurements, while the vertical error bars represent the corresponding BTD uncertainty. For atmospheres with PWV $\leq$ 1.84 g cm^{-2}, the corrections are negative implying that the BTD slope for water vapor and dust is similar (see Figure 3). For these cases, the correction was added. For values of PWV > 1.84 g cm^{-2}, the BTD slope of water vapor and dust is of opposite sign and the correction was subtracted.

[46] Figure 6c shows the impact of PWV uncertainty on the AERI detection scheme for a mixed case of dust and cirrus assuming a PWV of 2.4 ± 0.1 g cm^{-2}. The top solid curve represents the BTD 11–10 for dust and cirrus before the corrections are applied. Note that for each dust optical depth, the BTD 11–10 lies above the zero-point threshold; hence dust will not be detected. For the specified range of PWV, adding the corrections from Figure 6b yields a range of the corrected BTD 11–10 shown by the broken curves. The correction effectively reduces the magnitude of BTD 11–10, but depending on the error in the PWV measurement. For example, if the retrieved PWV is on the high (H) and low (L) end (10%), dust may be overestimated and underestimated.

[47] To further compensate for uncertainties in PWV and detecting cloud and dust near the BTD 11–10 threshold, the algorithm accounts for high-frequency temporal instabilities in the BT spectra, an approach similar to the AERONET cloud screening procedure [*Smirnov et al.*, 2000]. This is accomplished by evaluating the change in the BTD slope during each AERI measurement where rapid changes are indicative of cloud transits. Last, in the event that cloud is misclassified as dust, we check to see if the magnitude of the BT subband spectrum averaged over the window domain exceeds a prescribed threshold taken to be 270 K on the basis of radiative transfer simulations. The algorithm labels the event as cloud when BT $\geq$ 270 K.

4.2. Optical Depth Retrieval Methodology

[48] The retrieval methodology relies on a statistical optimization approach whereby a search is conducted for the maximum likelihood that ΔBT (observed) takes on the functional form of ΔBT (calculated) evaluated over the prescribed subbands. The retrieval algorithm is given by minimizing a residual sum, χ^2, defined as follows:

$$\chi^2 = \sum_{i=a}^{b} \left[\ln\left(\Delta BT^i_{calc}(\tau, a_e, T, \nu) - \ln\left(\Delta BT^i_{aeri}(T, \nu)\right)\right)\right]^2 \quad (7)$$

where the summation is performed over subbands a to b and ΔBT is a function of optical depth (τ), effective radius (a_e), temperature (T), and wave number (ν). The retrieval is repeated for each cloud-free AERI measurement following the dust/cloud detection scheme to yield a best fit IR optical depth at 962 cm^{-1}. Other works utilizing this and similar approaches using thermal IR observations include *Rathke and Fischer* [2000] and *Pierangelo et al.* [2004].

[49] The retrieval methodology employs a LUT of modeled dust ΔBT for the dust microphysical models presented in section 2. To this end, a LUT is constructed for each critical dust parameter including 5 mineral compositions (quartz, kaolinite, kaolinite mixed with hematite, kaolinite mixed with carbonate, and the Volz dust model) and 3 particle shapes (compact hexagon, oblate spheroid, and sphere). This allows us to compare the performance of each dust model in terms of a best fit with the observed BT data. In the current scheme, particle size is not retrieved because of the relatively small variability in the window region. The IR optical depths of the modeled dust spectra were interpolated over a range extending from τ = 0.05–1.0 in steps of 0.10. The atmospheric profiles used in the retrieval scheme were based on model clear-sky calculations using the combined AERIPLUS derived state parameters and MAARCO sounding data (section 3). Since the model clear-sky is continuously updated for each AERI observation, PWV is no longer considered a free parameter in the retrieval. Finally, it should be noted that the present retrieval

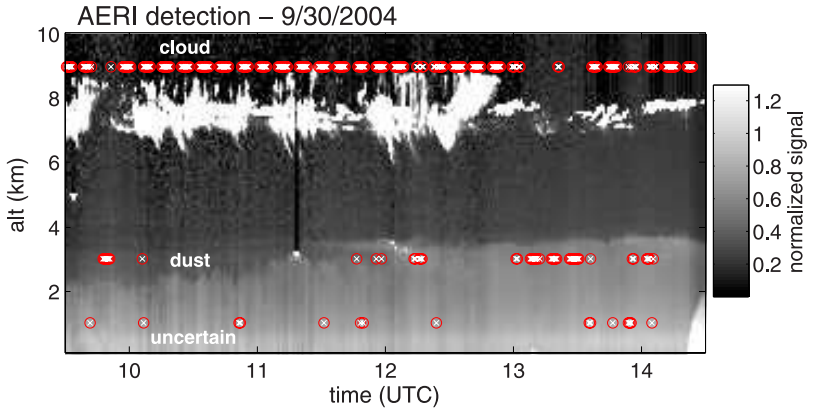

Figure 11. AERI detected cloud/dust versus MPL for 30 September 2004. "Cloud," "dust," and "uncertain" classifications are given by the top, center, and bottom rows, respectively. White/red markers represent detection with/without estimated nonlinearity applied. See text for details.

scheme also accounted for local temporal changes in the ambient surface temperatures by subtracting a BT thermal offset from each subband where a table of thermal corrections was constructed by differencing the clear-sky spectrum for a range of local times ranging from 0600 to 1700 UTC with a reference "cold" spectrum at 0600 UTC.

4.3. UAE^2 Case Studies

[50] Two cases from the UAE^2 were selected to illustrate the potential of the detection/retrieval methodology: 22 September and 30 September 2004 during which prevalent dust and cirrus cloud conditions occurred, respectively. We first demonstrate the strength of the dust detection approach. Figure 11 shows the SMART MPLNET micropulse lidar (MPL) normalized relative backscatter (NRB) signal described by *Campbell et al.* [2002] for 30 September 2004. Note the persistent cirrus cloud coverage from 0930 to 1430 UTC interrupted by several small breaks at 0950 UTC, 1300–1330 UTC and 1400 UTC. The AERI detection results are given by the red and white labels where the top, center and bottom rows represent cloud, dust and uncertain conditions (i.e., near the BTD 11–10 zero point), respectively. The colors indicate AERI data with (white) and without (red) the estimated MgCdTe nonlinearity corrections applied. As shown by the positions of the labels, the results are not sensitive to the estimated error and were found to be within 1% of each other. Consistent with the MPL, the AERI algorithm detected mostly cirrus with some dust at each cloud break (~80% and 17% of the AERI observations, respectively). Several points around 1200 UTC were also identified as dust in the presence of cirrus.

[51] Next, we tested the dust retrieval technique using cloud-screened AERI radiances from 22 September during the 4-h period 0600–1000 UTC. We performed the retrieval employing the channel 1 AERI data set with and without the estimated MgCdTe nonlinearity corrections. Figure 12a shows the AERI retrieved IR optical depths at 962 cm^{-1} (10.4 μm) assuming a spherical Volz dust model with an effective radius of 1 μm. The gray and black curves at the bottom are the data with and without corrections, respectively. If the MgCdTe detector nonlinearity is not accounted for, the mean estimated error in the retrieved optical depths would range from ~3–5% over the 4-h period. For comparison are the AERONET retrieved visible optical depths (top curve) at 0.55 μm. Note the similar trend in the retrieved optical depths of each instrument. The AERI optical depths were then scaled to 0.55 μm for direct comparison with AERONET using the Volz visible-to-IR

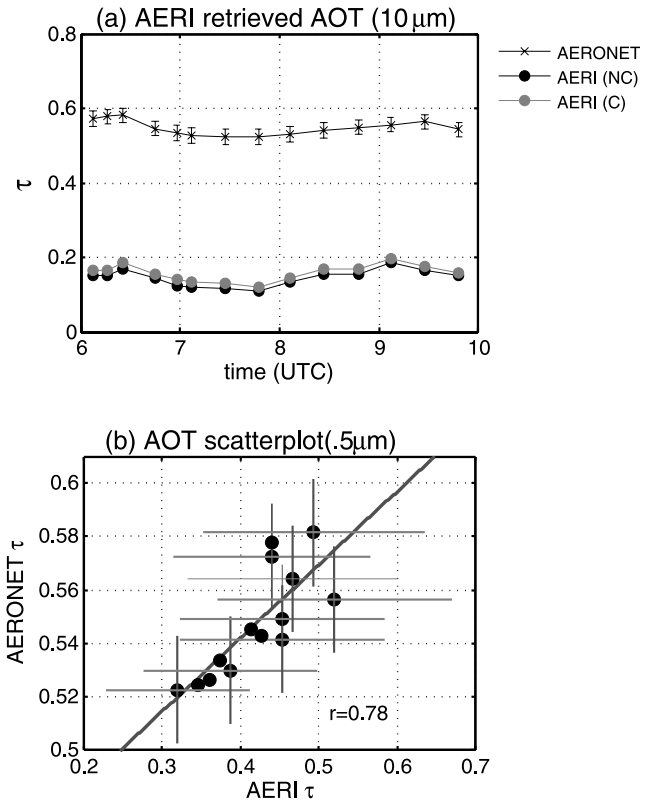

Figure 12. (a) AERI retrieved IR optical depths for 22 September 2004 with/without nonlinearity corrections applied (NC, not corrected; C, corrected). (b) AOT scatterplot of AERI versus AERONET retrieved optical depths at 0.5 μm. See text for details.

extinction coefficient ratio ($\beta_{0.55\mu m}/\beta_{10.4\mu m}$) which varies from 2 to 3 for dust particle sizes in the range of 0.75–1.5 μm. The scatterplot in Figure 12b shows the linear trend between the scaled AERI and the AERONET optical depths with a correlation coefficient of 0.78, indicating the retrieval is able to capture the temporal variability in the dust load with some success. The horizontal and vertical error bars depict the variability in the retrieved optical depths due to AERONET retrieval and AERI particle sizing uncertainties, respectively. Note that the AERI retrieved optical depths agree with those from AERONET within the uncertainty estimates.

5. Summary

[52] Detailed sensitivity studies to key dust and atmospheric parameters in the thermal IR window were conducted to examine the potential for developing methodologies to detect and retrieve dust aerosol using ground-based AERI BT spectra during the UAE^2. To this end, dust microphysical models characterizing mineral composition, particle shape, and size were constructed by combining in situ data from the UAE^2 with that from prior field studies. Using FDTD and T-matrix light scattering codes, the dust single-scattering properties were calculated and found to be most sensitive to the refractive index of component minerals, consistent with previous studies. Comprehensive studies of uncertainties in water vapor measurements and its vertical variability were critically analyzed in the thermal IR window for their impact on AERI applications. Results indicated (1) a 10% measurement uncertainty in PWV amounts to an error in the averaged clear-sky BT spectra of $\sim\pm4-6$ K, corresponding to a dust visible (0.55 μm) optical depth of $\sim$0.15, and (2) uncertainties in the vertical distribution of water vapor and temperature for cases not associated with strong weather systems, resulted in BT errors between $\sim1-3$ K in the averaged spectra. Consequently, a dynamic BTD clear-sky correction was formulated for dust detection and the AERIPLUS retrieved temperature and relative humidity profiles were employed to characterize the time-dependent thermodynamic state of the lower troposphere for dust retrieval. The vertical variability in temperature and the large surface temperature gradients measured during UAE^2 also necessitated the need for a thermal correction in the retrieval methodology.

[53] Detailed sensitivity studies of critical dust parameters revealed significant effects on the AERI BT spectra. Unique to AERI detection was the BTD 11–10 dynamic threshold, which exploits the differences in the absorptive properties of minerals and liquid/ice water for separating dust from cloud. The BTD 11–10 for dust was shown to be negative while that for clouds was positive. Most common minerals except for pure calcium carbonate exhibit this effect. Water vapor causes BTD 11–10 to increase which can cause dust to be underestimated. Particle size and shape effects on the AERI spectra using compact hexagons, oblate spheroids and spheres for sizes in the range of 0.5–2 μm exhibited unique spectral dependence over the subbands and were found to increase with dust optical depth. Independent of shape, the potential strength for particle size separation in the window region appears more likely for particles less than 1 μm with decreasing sensitivity toward 2 μm. For the cases analyzed, compact hexagons showed the greatest sensitivity which emphasizes the significance of particle asphericity in dust remote sensing applications. AERI sensitivity to dust optical depth displays strong subband slope dependence particularly around 1100–1200 cm^{-1} for most minerals including quartz and the kaolinite/carbonate dust mixture. Investigation of the AERI sensitivity to dust layer altitude and thickness shows a significant impact on the vertical distribution of dust optical depths. The spectra in elevated dust layers were found to be reduced in magnitude between 2 and 10 K for the range of optical depths 0.05–0.4. The largest spectral change to dust thickness occurs in the first two layers ($\sim$8–10 K) and is reduced in the remaining layers with relative differences amounting to $\sim$2–5 K.

[54] On the basis of the sensitivity results, a combined detection/retrieval methodology was formulated and tested using two daytime dust and cirrus cases from the UAE^2. Consideration to the MgCdTe detector nonlinearity was addressed to examine the methodology's sensitivity to the estimated errors. By comparing the detection/retrieval results with collocated AERONET Sun photometer/MPLNET micropulse lidar measurements, we illustrated that the present scheme can be used to separate dust from cloud, and retrieve dust IR optical depths during daytime conditions with some confidence; that is, (1) the AERI and AERONET retrieved optical depths correlate well (r^2 = 78%) and show good agreement, well within the experimental uncertainties and (2) consistent with the MPL results, about 80% of the total AERI observations were classified as cloud while dust amounted to about 17% of the observations. Comparison of the detection results with and without the estimated MgCdTe detector nonlinearity corrections, revealed small differences (<1%), although this did increase the magnitude of the retrieved optical depths on average between $\sim$3–5%. Further constraints in the AERI dust detection approach can be achieved by integrating cloud observations from coincident ground and satellite-based platforms, including those from the "A-Train" satellite constellation (e.g., AIRS and CALIPSO synergy) and collocated lidar systems. A forthcoming paper will address application of the present methodology using the corrected UAE^2 AERI data set along with implications for computing the region's longwave dust surface radiative forcing.

[55] **Acknowledgments.** We are grateful to the Department of Water Resources, Office of the President (DWRS-United Arab Emirates), and Stuart Piketh (University of the Witwatersrand, Johannesburg, South Africa) for their logistical support and making this field study possible. We thank B. Kahn and A. Eldering at JPL/Caltech for making the CHARTS program available through AER. We also thank C. Zender (UCI) and T. Roush (NASA AMES) for making the mineral data sets available. The NASA Micropulse Lidar Network was funded by the NASA Earth Observing System and Radiation Sciences Program, and the AERONET site is maintained by B. Holben. We also thank J. Campbell for providing the SMART MPL data and W. Feltz for making available the AERIPLUS retrieval algorithm. Last, we are grateful to the reviewers of this manuscript for their helpful and insightful comments. J. S. Reid's participation was provided by the Office of Naval Research Code 322. This research was supported by NASA grants NNC5–712 and NNG04GG91G and DOE grant DOE-FG03-00ER62.

References

Aba-Husayn, M. M., and A. H. Sayegh (1977), Mineralogy of Al-Hasa desert soils (Saudi Arabia), *Clays Clay Miner.*, *25*, 138–147, doi:10.1346/CCMN.1977.0250211.

Bruegge, C. T., J. E. Conel, R. O. Green, J. S. Margolis, R. G. Holm, and G. Toon (1992), Water vapor column abundance retrieval during FIFE, *J. Geophys. Res.*, *97*, 18,759–18,768.

Campbell, J. R., D. L. Hlavka, E. J. Welton, C. J. Flynn, D. D. Turner, J. D. Spinhirne, V. S. Scott, and I. H. Hwang (2002), Full-time, eye-safe cloud and aerosol lidar observation at Atmospheric Radiation Measurement program sites: Instruments and data analysis, *J. Atmos. Oceanic Technol.*, *19*, 431–442, doi:10.1175/1520-0426(2002)019<0431:FTESCA>2.0.CO;2.

Clough, S. A., F. Kneiyzs, and R. Davis (1989), Line shape and the water vapor continuum, *Atmos. Res.*, *23*, 229–241, doi:10.1016/0169-8095(89)90020-3.

Clough, S. A., M. J. Iacono, and J. L. Moncet (1992), Line-by-line calculations of atmospheric fluxes and cooling rates. Application to water vapor, *J. Geophys. Res.*, *97*, 15,761–15,785.

Deslover, D. H., W. L. Smith, P. K. Piironen, and E. W. Eloranata (1999), A methodology for measuring cirrus cloud visible to infrared spectral optical depth ratios, *J. Atmos. Oceanic Technol.*, *16*, 251–262, doi:10.1175/1520-0426(1999)016<0251:AMFMCC>2.0.CO;2.

DeSouza-Machado, S. G., L. L. Strow, S. E. Hannon, and H. E. Motteler (2006), Infrared dust spectral signatures from AIRS, *Geophys. Res. Lett.*, *33*, L03801, doi:10.1029/2005GL024364.

Dufresne, J. L., C. Gautier, and P. Ricchiazzi (2002), Longwave scattering effects of mineral aerosols, *J. Atmos. Sci.*, *59*, 1959–1966, doi:10.1175/1520-0469(2002)059<1959:LSEOMA>2.0.CO;2.

Feltz, W. F., W. L. Smith, H. B. Howell, R. O. Knuteson, H. Woolf, and H. E. Revercomb (2003), Near-continuous profiling of temperature, moisture, and atmospheric stability using the Atmospheric Emitted Radiance Inteferometer (AERI), *J. Appl. Meteorol.*, *42*, 584–597, doi:10.1175/1520-0450(2003)042<0584:NPOTMA>2.0.CO;2.

Grant, W. B. (1990), Water vapor absorption coefficients in the 8–13 - μm spectral region: A critical review, *Appl. Opt.*, *29*(4), 451–462.

Hansell, R. A., S. C. Ou, K. N. Liou, J. K. Roskovensky, S. C. Tsay, C. Hsu, and Q. Ji (2007), Simultaneous detection/separation of mineral dust and cirrus clouds using MODIS thermal infrared window data, *Geophys. Res. Lett.*, *34*, L11808, doi:10.1029/2007GL029388. (Correction, *Geophys. Res. Lett.*, *34*, L13802, doi:10.1029/2007GL031035, 2007.)

Highwood, E. J., J. M. Haywood, M. D. Silverstone, S. M. Newman, and J. P. Taylor (2003), Radiative properties and direct effect of Saharan dust measured by the C-130 aircraft during Saharan Dust Experiment (SHADE): 2. Terrestrial spectrum, *J. Geophys. Res.*, *108*(D18), 8578, doi:10.1029/2002JD002552.

Holben, H. B., et al. (1998), AERONET—A federated instrument network and data archive for aerosol characterisation, *Remote Sens. Environ.*, *66*, 1–16, doi:10.1016/S0034-4257(98)00031-5.

Hong, G., P. Yang, H.-L. Huang, S. A. Ackerman, and I. N. Sokolik (2006), Simulation of high-spectral-resolution infrared signature of overlapping cirrus clouds and mineral dust, *Geophys. Res. Lett.*, *33*, L04805, doi:10.1029/2005GL024381.

Intergovernmental Panel on Climate Change (2007), *Climate Change: The Physical Science Basis—Contribution of Working Group I to the Fourth Assessment Report of the Intergovernmental Panel on Climate Change*, Cambridge Univ. Press, New York.

Kahn, B. H., K. N. Liou, S. Y. Lee, E. F. Fishbein, S. DeSouza-Machado, A. Eldering, E. J. Fetzer, S. E. Hannon, and L. L. Strow (2005), Nighttime cirrus detection using Atmospheric Infrared Sounder window channels and total column water vapor, *J. Geophys. Res.*, *110*, D07203, doi:10.1029/2004JD005430.

Kalashnikova, O. V., and I. N. Sokolik (2004), Modeling the radiative properties of non-spherical soil-derived mineral aerosols, *J. Quant. Spectrosc. Radiat. Transfer*, *87*, 137–166, doi:10.1016/j.jqsrt.2003.12.026.

Knuteson, R. O., et al. (2004), Atmospheric Emitted Radiance Interferometer (AERI). Part II: Instrument performance, *J. Atmos. Oceanic Technol.*, *21*, 1777–1789, doi:10.1175/JTECH-1663.1.

Koren, I., E. Ganor, and J. H. Joseph (2001), On the relation between size and shape of desert dust aerosol, *J. Geophys. Res.*, *106*, 18,047–18,054, doi:10.1029/2000JD900558.

Kumar, A., P. J. Minnett, G. Podesta, and R. H. Evans (2003), Error characteristics of the atmospheric correction algorithms used in retrieval of sea surface temperatures from infrared satellite measurements: Global and regional aspects, *J. Atmos. Sci.*, *60*, 575–585, doi:10.1175/1520-0469(2003)060<0575:ECOTAC>2.0.CO;2.

Miller, S. D., A. P. Kuciauskas, M. Liu, Q. Ji, J. S. Reid, D. W. Breed, A. L. Walker, and A. A. Mandoos (2008), Haboob dust storms of the southern Arabian Peninsula, *J. Geophys. Res.*, *113*, D01202, doi:10.1029/2007JD008550.

Mishchenko, M. I., and L. D. Travis (1994), Light scattering by polydispersions of randomly oriented spheroids with sizes comparable to wavelengths of observation, *Appl. Opt.*, *33*, 7206–7225.

Mishchenko, M. I., and L. D. Travis (1998), Capabilities and limitations of a current Fortran implementation of the T-Matrix method for randomly oriented, rotationally symmetric scatterers, *J. Quant. Spectrosc. Radiat. Transfer*, *60*, 309–324, doi:10.1016/S0022-4073(98)00008-9.

Moncet, J. L., and S. A. Clough (1997), Accelerated monochromatic radiative transfer for scattering atmospheres: Application of a new model to spectral radiance measurements, *J. Geophys. Res.*, *102*, 21,853–21,866, doi:10.1029/97JD01551.

Moy, L., H. E. Revercomb, R. O. Knuteson, D. D. Turner, and E. Kassianov (2005), Retrieving aerosols from the Atmospheric Emitted Radiance Interferometer, paper presented at Fifteenth ARM Science Team Meeting, U.S. Dep. of Energy, Daytona Beach, Fla.

Nalli, N. R., et al. (2006), Ship-based measurements for infrared sensor validation during Aerosol and Ocean Science Expedition 2004, *J. Geophys. Res.*, *111*, D09S04, doi:10.1029/2005JD006385.

Okada, K., A. Kobayashi, Y. Iwasaka, H. Naruse, T. Tanaka, and O. Nemoto (1987), Features of individual Asian dust-storm particles collected at Nagoya, Japan, *J. Meteorol. Soc. Jpn.*, *65*, 515–520.

Okada, K., J. Heitzenberg, K. Kai, and Y. Qin (2001), Shape of atmospheric mineral particles collected in 3 Chinese arid regions, *Geophys. Res. Lett.*, *28*, 3123–3126, doi:10.1029/2000GL012798.

Parungo, F., et al. (1995), Asian dust storms and their effects on radiation and climate: Part 1, *STC Rep. 2906*, Sci. and Technol. Corp., Hampton, Va.

Pierangelo, C., A. Chedin, S. Heilliette, N. Jacquinet-Husson, and R. Armante (2004), Dust altitude and infrared optical depth from AIRS, *Atmos. Chem. Phys.*, *4*, 1813–1822.

Pierangelo, C., M. Mishchenko, Y. Balkanski, and A. Chédin (2005), Retrieving the effective radius of Saharan dust coarse mode from AIRS, *Geophys. Res. Lett.*, *32*, L20813, doi:10.1029/2005GL023425.

Rathke, C., and J. Fischer (2000), Retrieval of cloud microphysical properties from thermal infrared observations by a fast iterative radiance fitting method, *J. Atmos. Oceanic Technol.*, *17*, 1509–1524, doi:10.1175/1520-0426(2000)017<1509:ROCMPF>2.0.CO;2.

Realmuto, V. J., and H. M. Worden (2000), Impact of atmospheric water vapor on the thermal infrared remote sensing of volcanic sulfur dioxide emissions: A case study from the Pu'u 'O'o vent of Kilauea Volcano, Hawaii, *J. Geophys. Res.*, *105*, 21,497–21,508, doi:10.1029/2000JB900172.

Reid, E. A., J. S. Reid, M. M. Meier, M. R. Dunlap, S. S. Cliff, A. Broumas, K. Perry, and H. Maring (2003), Characterization of African dust transported to Puerto Rico by individual particle and size segregated bulk analysis, *J. Geophys. Res.*, *108*(D19), 8591, doi:10.1029/2002JD002935.

Reid, J. S., E. A. Reid, S. Piketh, S. Cliff, A. Al Mandoos, A. Walker, and S. C. Tsay (2008), Dynamics of Southwest Asian Dust Particle Size Characteristics with Implications for Global Dust Research, *J. Geophys. Res.*, *113*, D14212, doi:10.1029/2007JD009752.

Roskovensky, J. K., and K. N. Liou (2005), Differentiating airborne dust from cirrus clouds using MODIS data, *Geophys. Res. Lett.*, *32*, L12809, doi:10.1029/2005GL022798.

Roskovensky, J. K., K. N. Liou, T. J. Garrett, and D. Baumgardner (2004), Simultaneous retrieval of aerosol and thin cirrus optical depths using MODIS airborne simulator data during CRYSTAL-FACE and CLAMS, *Geophys. Res. Lett.*, *31*, L18110, doi:10.1029/2004GL020457.

Rothman, L. S., et al. (1992), The HITRAN molecular database: Editions of 1991 and 1992, *J. Quant. Spectrosc. Radiat. Transfer*, *48*, 469–507, doi:10.1016/0022-4073(92)90115-K.

Singer, A., S. Dultz, and E. Argaman (2004), Properties of the non-soluble fractions of suspended dust over the Dead Sea, *Atmos. Environ.*, *38*, 1745–1753, doi:10.1016/j.atmosenv.2003.12.026.

Smirnov, A., B. N. Holben, T. F. Eck, O. Dubovik, and I. Slutsker (2000), Cloud screening and quality control algorithms for the AERONET data base, *Remote Sens. Environ.*, *73*, 337–349, doi:10.1016/S0034-4257(00)00109-7.

Sokolik, I. N., and O. B. Toon (1999), Incorporation of mineralogical composition into models of the radiative properties of mineral aerosols from UV to IR wavelengths, *J. Geophys. Res.*, *104*, 9423–9444, doi:10.1029/1998JD200048.

Turner, D. D., S. A. Ackerman, B. A. Baum, H. E. Revercomb, and P. Yang (2003), Cloud phase determination using ground-based AERI observations at SHEBA, *J. Appl. Meteorol.*, *42*, 701–715, doi:10.1175/1520-0450(2003)042<0701:CPDUGA>2.0.CO;2.

Turner, D. D., H. E. Revercomb, R. O. Knuteson, R. G. Dedecker, and W. F. Feltz (2004), An evaluation of the nonlinearity correction applied to Atmospheric Emitted Radiance Interferometer (AERI) data collected by the Atmospheric Radiation Measurement Program, *DOE ARM Tech. Rep., TR-013*, 7 pp., U.S. Dep. of Energy, Washington, D. C.

Vogelmann, A. M., P. J. Flatau, M. Szczodrak, K. M. Markowicz, and P. J. Minett (2003), Observations of large aerosol IR forcing at the surface, *Geophys. Res. Lett.*, *30*(12), 1655, doi:10.1029/2002GL016829.

Volz, F. E. (1973), Infrared optical constants of ammonium sulfate, Sahara dust, volcanic pumice, and fly ash, *Appl. Opt.*, *12*, 564–568.

Waterman, P. C. (1971), Symmetry, unitarity and geometry in electromagnetic scattering, *Phys. Rev. D*, *3*, 825–839.

Welton, E. J., J. R. Campbell, J. D. Spinhirne, and V. S. Scott (2001), Global monitoring of clouds and aerosols using a network of micro-pulse lidar systems, *Proc. SPIE Int. Soc. Opt. Eng.*, *4153*, 151–158.

Yang, P., and K. N. Liou (1995), Light scattering by hexagonal ice crystals: Comparison of finite difference time domain and geometric optics models, *J. Opt. Soc. Am.*, *12*, 162–176.

Yang, P., H. Wei, H.-L. Huang, B. A. Baum, Y. X. Hu, G. W. Kattawar, M. I. Mishchenko, and Q. Fu (2005), Scattering and absorption property database for nonspherical ice particles in the near- through far-infrared spectral region, *Appl. Opt.*, *44*, 5512–5523, doi:10.1364/AO.44.005512.

Yee, S. K. (1966), Numerical solution of initial boundary value problems involving Maxwell's equation in isotropic media, *IEEE Trans. Antennas Propag.*, *14*, 302–307.

R. A. Hansell and Q. Ji, Earth System Science Interdisciplinary Center, University of Maryland, College Park, MD 20740, USA. (richard.a.hansell@nasa.gov)

K. N. Liou and S. C. Ou, Department of Atmospheric and Oceanic Sciences, University of California, Los Angeles, CA 90095, USA.

J. S. Reid, Naval Research Laboratory, Monterey, CA 93943, USA.

S. C. Tsay, NASA Goddard Space Flight Center, Greenbelt, MD 20771, USA.